Carbon 102 (2016) 357–366

Contents lists available at ScienceDirect

Carbon

journal homepage: www.elsevier.com/locate/carbon

Synthesis and characterization of composite membranes made of graphene and polymers of intrinsic microporosity

Yuyoung Shin [a], Eric Prestat [b], Kai-Ge Zhou [a], Patricia Gorgojo [c], Khalid Althumayri [a], Wayne Harrison [a], Peter M. Budd [a], Sarah J. Haigh [b], Cinzia Casiraghi [a, *]

[a] School of Chemistry, University of Manchester, Manchester, M13 9PL, UK
[b] School of Materials, University of Manchester, Manchester, M13 9PL, UK
[c] School of Chemical Engineering and Analytical Science, University of Manchester, Manchester, M13 9PL, UK

ARTICLE INFO

Article history:
Received 2 December 2015
Received in revised form
9 February 2016
Accepted 11 February 2016
Available online 16 February 2016

ABSTRACT

Polymers of intrinsic microporosity (PIMs) are a group of polymers with molecular sieve behaviour due to their rigid, contorted macromolecular backbones. They show great potential in organophilic pervaporation, solvent-resistant nanofiltration and gas and vapour separations. However, they are susceptible to physical ageing, leading to a reduction in permeability over time. An improvement in membrane permeability, control over diffusion selectivity and a reduction of the effect of physical ageing is expected by adding graphene as a nanofiller.

Little is experimentally known about how the material disperses in the polymer. Here we used Raman spectroscopy, scanning transmission electron microscopy (STEM) and electron energy loss spectroscopy (EELS) to study the composite membrane's structure. Our results show that both STEM and Raman spectroscopy are able to identify the presence of graphene-based material in the composite. We show that STEM, through medium angle annular dark field (MAADF) or EELS imaging, can be exploited to obtain information on the morphology and the thickness of the flakes. Our results indicate that there is strong re-agglomeration of initially exfoliated graphene in solution when forming the composite. This is expected to produce strong changes in the mechanical properties and the physical ageing of the membrane.

© 2016 The Authors. Published by Elsevier Ltd. This is an open access article under the CC BY license (http://creativecommons.org/licenses/by/4.0/).

1. Introduction

Graphene is a two dimensional allotrope of sp^2 bonded carbon atoms in a hexagonal honeycomb structure, or more simply, a single layer of graphite [1]. Graphene has attracted great interest due to its remarkable properties, such as high charge mobility [2–4], thermal conductivity [5], and mechanical stability and elasticity [6]. Micro-mechanical exfoliation (MME) of graphite is a relatively simple and low cost method, but this process is not mass-scalable and therefore not compatible with industrial needs [7].

Amongst several methods of graphene production, liquid-phase exfoliation (LPE) shows great potential as a mass-scalable and low-cost approach for industrial production [7–9]. Furthermore, it can be extended to other 2D crystals [10]. Although LPE graphene is considered to be of "poor quality" for applications in electronics [7,11], it shows great potential in other applications: it can be used as inks, paints, and for production of membranes and composites [7]. In particular, mixing a nano-level dispersion of graphene platelets in a polymer matrix is a simple and cost-effective method that can bring significant improvement to the properties of the polymer. The high surface-to-volume ratios, relatively low production cost, and the unique properties of graphene make this material very attractive as a filler for composites.

In this work, we have investigated a new class of polymers to combine with graphene: polymers of intrinsic microporosity (PIMs) [12]. These are obtained by forming a backbone that has no freedom to change conformation, yet is sufficiently contorted to prevent dense packing [13]. Here we focus on highly fluorescent spiropolymer, PIM-1, whose structure is shown in Fig. 1. PIM-1 shows particularly high molecular mass and good solubility amongst various members of PIMs [12]. Despite its rigid structure, PIM-1 is freely soluble in some organic solvents, allowing conventional solution-based polymer processing techniques to be

* Corresponding author.
E-mail address: cinzia.casiraghi@manchester.ac.uk (C. Casiraghi).

http://dx.doi.org/10.1016/j.carbon.2016.02.037
0008-6223/© 2016 The Authors. Published by Elsevier Ltd. This is an open access article under the CC BY license (http://creativecommons.org/licenses/by/4.0/).

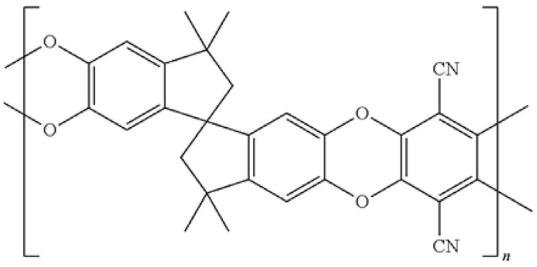

Fig. 1. Structure of PIM-1.

applied, *i.e.* robust, self-standing films of high optical clarity and high surface area can be prepared simply by casting from solution [12]. Moreover, the microporous structure and the chemical functionalities of PIM-1 create a high capacity for gas uptake, with high gas permeability and high selectivity [12,14–16], and makes this material highly suitable for use in organophilic pervaporation [17,18] and solvent-resistant nanofiltration [19,20].

PIM-1, like other highly permeable glassy polymers, is also susceptible to physical ageing [21]. This is caused by the decrease in the free volume over time and can lead to decay of the membrane's permeation performance. The addition of a nanofiller such as graphene can help to reduce this detrimental structural change [22]. Moreover, carbon-based nanofillers in PIM-1 have been shown to improve the membrane permeability and to provide control over diffusion selectivity [23,24]. The effect of the nanofiller, however, is expected to depend strongly on how it interacts with the polymer. For LPE graphene, this will also depend on the properties of the dispersion, such as the concentration of graphene and size and thickness distribution of the nanosheets.

Characterization of the structural morphology is, therefore, crucial to gain an effective understanding of the structure-property relationships of the composite. Obtaining such structural information, however, is experimentally challenging. For example, it may be difficult to detect the Raman signal of graphene due to the typical fluorescence produced by the polymer, damage may be observed due to the laser power or the signal of graphene may not be detectable, in particular at very low filler concentration. In the cases of TEM and STEM, very little contrast is typically obtained: traditional diffraction contrast imaging requires flakes to be correctly oriented with respect to the electron beam and has a poor signal to noise ratio due to the weak diffraction in the graphene nanosheets relative to the much greater volume of amorphous PIM-1 matrix material. The popular high angle annular dark field (HAADF) STEM imaging mode also shows poor contrast as a result of the similar atomic numbers of graphene and PIM-1. On top of that, the preparation of a representative, suspended film sample thin enough to allow TEM or STEM imaging presents practical difficulties.

In this work we demonstrate the first extensive characterisation of PIM-1/Graphene (PIM-1/Gr) composites using Raman spectroscopy and STEM imaging. Raman spectroscopy shows that the filler is not single-layer, but most likely composed of re-aggregated graphene flakes, with restacking occurring either in the initial dispersion or during the formation of the membrane as solvent evaporates. STEM investigations confirm these results and bring deeper insights into the morphology of the graphene flakes as well as their distribution within the polymer matrix. We also show that EELS can be used to get precise structural information regarding the flakes morphology, the presence of defects and the number of layers. Our results suggest that higher graphene concentration could be detrimental to the composite properties of the material, as this will increase the tendency of the flakes to restack. Lower concentrations (<0.05 mg/ml for the typical volumes used in this work) are expected to minimize the risk of restacking and could also improve permeability, by increasing the polymer free volume.

2. Experimental

2.1. Material preparation

Pure graphene dispersions were prepared by adding 6 mg/ml of graphite (Graphexel ltd.) to 100 ml of chloroform (Sigma–Aldrich), bath-sonicating for 84 h and then centrifuging the solution at 10000 rpm (7378 g) for 20–30 min. After centrifugation, only the top layer of the well-dispersed solution was preserved for further investigation. We used similar conditions (sonication time, power, etc) as reported in previous works on liquid-phase exfoliation [8,10].

Fig. 2 summarises the method used to prepare the PIM-1/Gr composites. To produce the PIM-1/graphene composite dispersion, PIM-1 powder, prepared following the low-temperature method described in Ref. [25] was dissolved in chloroform and then processed following a similar process as described for the pure graphene dispersions, but with a sonication time of 72 h and a centrifugation time of 30 min. Pure PIM-1 and PIM-1/Gr composite membranes were prepared by simple casting of the solutions in glass petri dishes and allowing the solvent to evaporate under ambient conditions.

2.2. Characterization

2.2.1. UV–Vis spectroscopy

The final concentration of graphene in the dispersions (both pure graphene and the PIM-1/Gr composites) was determined using UV–Vis spectroscopy. The UV–Vis spectrum of graphene appears flat and featureless in the visible-IR region [8], so the absorption is measured at 660 nm for estimation of the graphene nanosheet concentration using the Beer–Lambert law. Despite the extensive work done towards accurately estimating the absorption coefficient, this is still the subject of considerable debate, showing much variance in different studies [26]. Throughout this study, an absorption coefficient of 2460 L g^{-1} m^{-1} was used for estimating the graphene concentration [27–29]. A Perkin–Elmer l-900 UV–Vis–NIR spectrophotometer was used to acquire the spectra.

2.2.2. Raman spectroscopy

Raman measurement was performed using a Renishaw Invia Raman spectrometer equipped with 514 nm and 633 nm excitation lines and a 1.0 mW laser power. Pure graphene dispersions were drop cast onto silicon substrates and Raman measurements were taken with 514 nm laser, 100X NA0.85 objective lens and 2400 grooves/mm grating. PIM-1/Gr composite samples were measured with 633 nm laser and 1200 grooves/mm grating. In the case of the composite materials, the samples were drop-cast or spin-coated onto a silicon substrate. Typically 20–50 Raman spectra were obtained for each sample.

2.2.3. STEM

The samples were obtained by first spin coating the dispersion onto a glass substrate, then immersing the sample in deionized water, causing the film to float off the glass and become suspended on the surface of the water. The thin composite membrane was then fished from the surface onto a holey carbon mesh or Quantifoil TEM support grid.

Aberration corrected STEM and EELS imaging were performed on a FEI Titan 80–200 ChemiSTEM equipped with a probe-side aberration corrector and an X-FEG electron source. The

Fig. 2. Schematic of the LPE process used to prepare PIM-1/graphene dispersions. (A colour version of this figure can be viewed online.)

experiment was performed using an acceleration voltage of 200 kV, a beam current of 150 pA and a convergence angle of 21 mrad. EEL spectra were acquired using a GIF Quantum with an energy dispersion of 0.1 eV and a collection angle of 62 mrad, providing an effective energy resolution of 1.2 eV. The pixel time used for EEL spectrum imaging was 50 ms. For STEM imaging, different detector configurations were used: in standard imaging mode, the bright field (BF)- and medium angle annular dark field (MAADF) collection angles were 0–8 mrad and 33–162 mrad respectively, while in spectroscopy imaging mode the high-angle-annular-dark-field (HAADF) collection angle was 62–140 mrad.

The planar sp^3 content is defined as $I_{\sigma^*}/(I_{\sigma^*}+ I_{\pi^*})$ with I_{σ^*} and I_{π^*} being the σ^* and π^* peak intensities respectively, obtained by fitting Gaussian functions to the corresponding peaks in the EELS C–K edge [30]. Data analysis has been performed using Python and the HyperSpy library [31]. The thickness of the specimen was measured using the EELS log-ratio technique [32]. The inelastic mean free path was calculated using the method of Iakoubovskii *et al.* and assuming a density of PIM-1 of 0.85 g cm^{-3} [33].

3. Results and discussion

3.1. PIM-1/graphene dispersions

Three sets of PIM-1/graphene dispersions with different composition ratio were produced (Table 1). In set A, the total initial concentration of PIM-1 and graphite was held constant at 12 mg/ml for five different composition ratios between PIM-1 and graphite (PIM-1/Gr). Additionally, graphene dispersion in chloroform without PIM-1 is included in set A and labelled as sample A0. In set B, the initial concentration of PIM-1 was held constant at 15 mg/ml and different ratios were obtained by changing the initial graphite concentration. Note that in set B, the concentration of PIM-1 was determined as the optimum PIM-1 concentration to form a uniform membrane in a glass petri dish by simple casting. In set C, the initial graphite concentration was held constant at 1.2 mg/ml for four different composition ratios. This set was made with lower initial graphite concentration as we observed, when preparing sets A and B, that the use of smaller amount of graphite produces more stable composite dispersions (Table 1).

Fig. 3 shows images of the dispersions obtained and the corresponding composite membranes. Note that PIM-1 has a fluorescent yellow-green colour so the dispersion changes from yellow-green to dark-green, to nearly black, depending on the relative concentration of graphene nanosheets. The concentration of the graphene nanosheets in the dispersions was estimated using UV–Vis absorption spectroscopy. PIM-1 shows strong absorbance between 200 nm and 500 nm, but no absorbance around 660 nm (Fig. 4). Therefore, the graphene concentration, $C_{Graphene}$, is estimated by measuring the absorption at 660 nm and using an extinction coefficient of 2460 L g^{-1} m^{-1} [27–29].

For comparison, graphene dispersions were also made without PIM-1 using exactly the same process. The typical concentration of graphene nanosheets obtained for these control solutions was very small (Table 1, sample A0). This is in agreement with LPE theory, which places chloroform in the list of "poor solvents" [34]. In the framework of LPE, a solvent is able to effectively exfoliate graphite only when its surface tension is close to the surface tension of graphene (35–45 mJ m^{-2}) [8]. Chloroform has a surface tension of 27 mJ m^{-2} at ambient conditions [35]; therefore, this solvent is not able to provide a high yield of stable graphene nanosheets in dispersion. However, chloroform is one of a few solvents in which PIM-1 is soluble [12,36].

Table 1 also shows the graphene exfoliation yield, which is calculated as the ratio between the concentration of graphene measured by absorption spectroscopy and the concentration of

Table 1
Concentration of PIM-1, graphite and graphene for each sample produced in this work. In Set A the total initial concentration of PIM-1, $C_{i,PIM-1}$, and graphite, $C_{i,Graphite}$, was kept constant; In Set B, $C_{i,PIM-1}$ was kept constant; In Set C, $C_{i,Graphite}$ was kept constant. The exfoliation yield was calculated as the ratio between the concentration of graphene measured in the dispersion and the amount of graphite used ($C_{Graphene}/C_{i,Graphite}$). Volume ratio between graphene and PIM-1 is shown in percentage.

Set	Gr:PIM-1	$C_{i,graphite}$ (mg/ml)	$C_{i,PIM-1}$ (mg/ml)	$C_{f,graphene}$ (mg/ml)	Yield (%)	Volume ratio (%)	Stability
A0	100:0	12.0	0.0	0.032	0.27		Sedimentation
A1	95:5	11.4	0.60	0.40	3.5	32	Stable
A2	70:30	8.40	3.60	0.21	2.5	2.8	Stable
A3	50:50	6.02	6.02	0.14	2.3	1.1	Stable
A4	30:70	3.60	8.42	0.23	6.4	1.3	Stable
A5	5:95	0.62	11.4	0.04	6.4	0.17	Stable
B1	95:5	285	15.0	1.32	0.46	4.2	Sedimentation
B2	70:30	35.0	15.0	0.49	1.4	1.6	Sedimentation
B3	50:50	15.0	15.0	0.42	2.8	1.3	Sedimentation
B4	30:70	6.43	15.0	0.31	4.8	0.99	Sedimentation
B5	5:95	0.79	15.0	0.05	6.3	0.16	Sedimentation
C1	10:90	1.21	10.8	0.031	2.6	0.14	Stable
C2	20:80	1.22	4.82	0.048	4.0	0.48	Stable
C3	30:70	1.20	2.79	0.018	1.5	0.31	Stable
C4	70:30	1.20	0.52	0.023	1.9	2.1	Stable

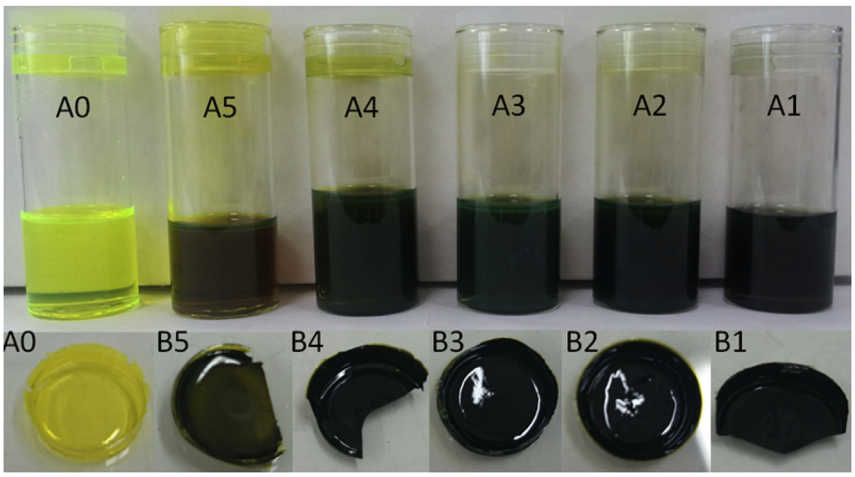

Fig. 3. a) Optical pictures of PIM-1/graphene dispersions (top) and membranes (bottom) studied in this work (Table 1). (A colour version of this figure can be viewed online.)

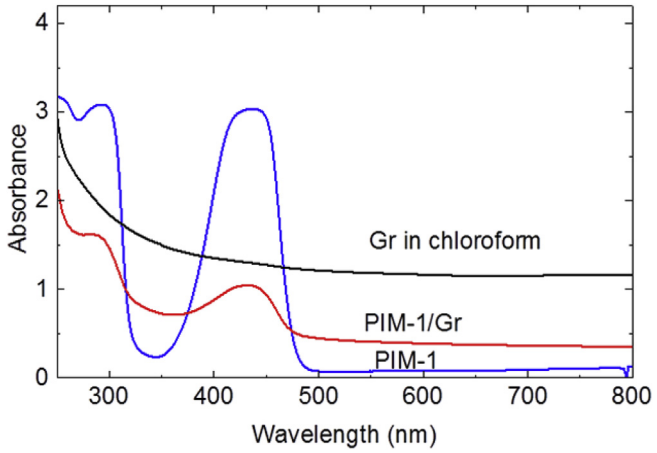

Fig. 4. Typical UV–Vis spectrum of diluted (x32) PIM-1/graphene dispersion (A5) compared with those of pure PIM-1 solution and pure graphene solution in chloroform. (A colour version of this figure can be viewed online.)

graphite added to the solution. In the ideal case of perfect exfoliation, the concentration of graphene would be equal to that of initial graphite (*i.e.* yield equal to 100%). Compared to the graphene dispersion made without any PIM-1 addition (*i.e.* sample A0), addition of just 0.6 mg/ml of PIM-1 (*i.e.* sample A1) increased the yield by a factor of ~13, showing that even a small concentration of PIM-1 is able to improve the exfoliation of graphite. However, one also has to note that in set A, the amount of starting graphite is not fixed: the highest graphene yield is obtained for samples A4 and A5, where the minimum amount of graphite was used in the initial dispersion (Table 1). Increasing the initial graphite loading leads to a higher final concentration of graphene in the membrane, but only at the expense of reduced exfoliation efficiency and an increased amount of wasted graphite. This observation is even more evident in set B, where the PIM-1 concentration is held constant (Table 1). The exfoliation yield is higher when a smaller amount of graphite is used (Samples B4 and B5). Note that sedimentation was not observed for any of the dispersions in set A (except sample A0) for approximately 3 months at ambient conditions.

Note that the enhancement of graphene exfoliation could be achieved through stabilization of graphene sheets in the solution via π-π interactions between the graphene sheets and PIM-1 hexagonal π-ring. Molecular simulations between graphene sheets and PIM-1 polymer matrix have shown good interface adhesion between the graphene sheets and polymer molecules, although most PIM-1 chain fragments were constrained due to the whole rigid chain structure [23]. However, this simulation was done for the polymer packed in a membrane, while in solution there could be more adhesive interactions between freely moving PIM-1 molecules and graphene sheets. Furthermore, the interaction molecule-solvent is expected to dominate the exfoliation process [37], therefore more modelling is needed to get further insights on the exfoliation process with PIM-1.

Finally we observed that when only a small amount of starting graphite is used (e.g. similar conditions to sample A5, or set C samples) the dispersions are neither yellow nor dark green, but instead have a clear brown colour (Fig. 5). For these samples, the yield can be quite high, giving graphene concentrations in the final dispersion of 0.01–0.04 mg/ml (Table 1). The strong colour difference may be an indication of different dispersion and/or interaction

Fig. 5. Photograph of PIM-1/graphene composite dispersions with different colours: (a) diluted (x2) A5 with volume ratio of Gr:PIM-1 = 0.17 and (b) C1 with volume ratio of Gr:PIM-1 = 0.14. (A colour version of this figure can be viewed online.)

of graphene within PIM-1. The distribution of graphene within the polymer is also expected to be dependent on the strength of interactions between the individual graphene nanosheets (*i.e.* re-stacking), which is strong in chloroform solutions due to the poor stabilization properties of the solvent. Therefore, by working at low concentration of graphene, it may be possible to improve the interaction of graphene with the polymer by minimizing re-stacking of graphene. Note that the change in colour is not due to any structural damage in the polymer, as PIM-1 peaks are clearly observed in the absorption spectra and diluted dispersions show the typical fluorescent green colour of PIM-1.

3.2. Raman characterization of PIM-1/graphene composite

Raman spectroscopy is a very powerful technique for the characterization of graphene [38,39]. This technique is able not only to identify graphene [40], but also to quantitatively probe defect concentrations [41,42], doping [43], strain [44,45] and so on. Note however that Raman results of MME graphene cannot be fully generalised to LPE graphene. The Raman spectrum of LPE graphene can be strongly affected by the exfoliation process: during sonication, the nanosheets are subjected to strong mechanical stress originating from the process of formation and collapse of bubbles and voids in the liquid. This ultimately breaks the flakes into smaller and thinner pieces in direct contact with the solvents. There are two major differences between the Raman spectrum of LPE and MME graphene. Firstly, the first order Raman spectrum of LPE graphene is typically characterized by the D peak [8], which is activated by the edges of the nanosheets having the size of nanosheet comparable to that of the laser spot [46]. The second difference relates to the 2D peak, which is typically used for identification of single-layer MME graphene [40]. LPE graphene shows a more complex lineshape [47–50], which may be caused by structural changes, but also by re-stacking of the flakes. Natural graphite is characterized by AB-stacking, but the nanosheets in the dispersion will re-stack in random stacking, giving complex 2D peak lineshapes as observed in a twisted bilayer [51,52].

In previous studies [48–50], we used a simple qualitative method based on the shape of the 2D peak to distinguish between single-layer graphene (SLG), few-layer sheets (FLG, restacked or retaining AB stacking) and graphitic material (>10 layers with AB stacking). This method is based on the evaluation of the coefficient of determination R^2, when fitting the peak with a Lorentzian lineshape: the closer to a perfect symmetric single peak (R^2 very close to 1), the higher the probability the nanosheet is a single-layer, while an asymmetric shape (low R^2) is used to identify few layers. Graphitic (*i.e.* unexfoliated) nanosheets have characteristic peak shape, given by (at least) two components, typical of bulk graphite with its natural AB stacking [40]. We have tested this method with several dispersions and processing conditions: our previous results have shown that the qualitative Raman analysis obtained following this protocol is in agreement with the results obtained by TEM [48–50].

Dispersions were drop cast onto silicon and 20–50 isolated flakes were measured for each dispersion described in Table 1. Fig. 6 shows typical Raman spectra obtained for LPE graphene in chloroform (without PIM-1, sample A0). As expected, the first order Raman spectrum shows a clear D peak, with an intensity ratio between D and G peaks typically below 2, as observed in similar dispersions [50]. By analysing the shape of the 2D peak with our protocol, we observed that the dispersion does not contain any single-layer material, and is mostly composed of few- and thick layers. This is in agreement with LPE theory, which places chloroform as “poor solvent for LPE of graphite” [8].

Raman spectroscopy of PIM-1/Gr composites is challenging because of PIM-1 strong photoluminescence, which hides the Raman signal, when measured at the most used laser excitation of 514 nm (Fig. 7(a)). However, by changing the wavelength of the laser, the photoluminescence can be easily removed from the spectral range of interest. Fig. 7(b,c) shows the Raman spectrum of PIM-1 measured at 633 nm: there are several Raman peaks in the region between 1300 and 1700 cm^{-1}, which partially overlap with the Raman features of LPE graphene. Therefore, in order to clearly see the G and D peak of graphene, the Raman spectrum of pure PIM-1 was subtracted from the Raman spectrum of PIM-1/Gr, using the PIM-1 peak at 1400 cm^{-1} to normalize the spectra. The spectra obtained in this way clearly shows the G and D peaks typical of LPE graphene (Fig. 7(b)). However, the first order Raman spectrum does not offer any information on the thickness of the graphene nanosheets. Analysis of the shape of the 2D peak at around 2700 cm^{-1} can provide thickness information. Because there are no PIM-1 Raman features in this region of the spectrum obtained with excitation energy at 633 nm (Fig. 7(c)), we can directly observe the 2D peak for the PIM-1/Gr membranes. This allows unambiguous identification of the presence of graphene nanosheets in the membrane by using Raman Spectroscopy. However, if the graphene concentration within the membrane is very low (*e.g.* set C), then the 2D peak may be hardly visible and very long measurements will be needed to resolve the 2D peak, with the risk of damaging the sample.

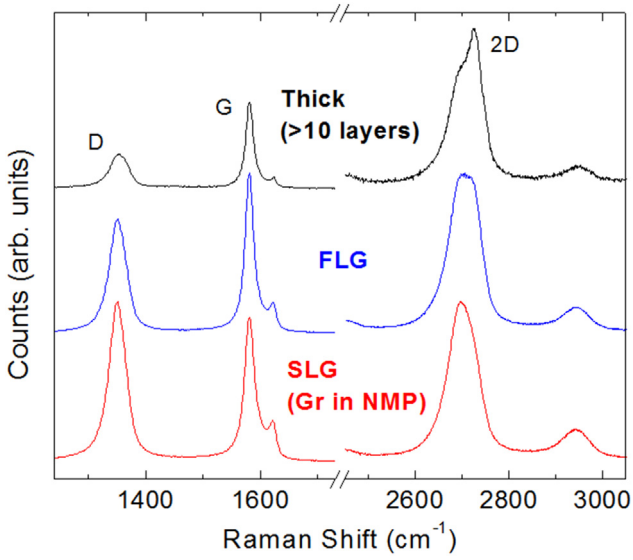

Fig. 6. Typical Raman spectra of LPE graphene in chloroform. For comparison, the typical Raman spectrum for SLG obtained from graphene dispersion in NMP is also shown. (A colour version of this figure can be viewed online.)

Fig. 7(c) shows that the 2D peak obtained for PIM-1/Gr composite samples are clearly asymmetric: the Lorentzian fit gives a R^2 coefficient always well below 0.99, indicating that none of the flakes is a single-layer. Graphitic material was also rarely observed: more than 95% of the Raman spectra of the PIM-1/Gr composites showed a 2D peak characteristic of re-stacked few layer graphene. Several methods were tested for membrane deposition including drop casting and spin coating. Although the films showed different surface morphology under the optical microscope, Raman spectroscopy did not show any strong difference between the different deposition techniques.

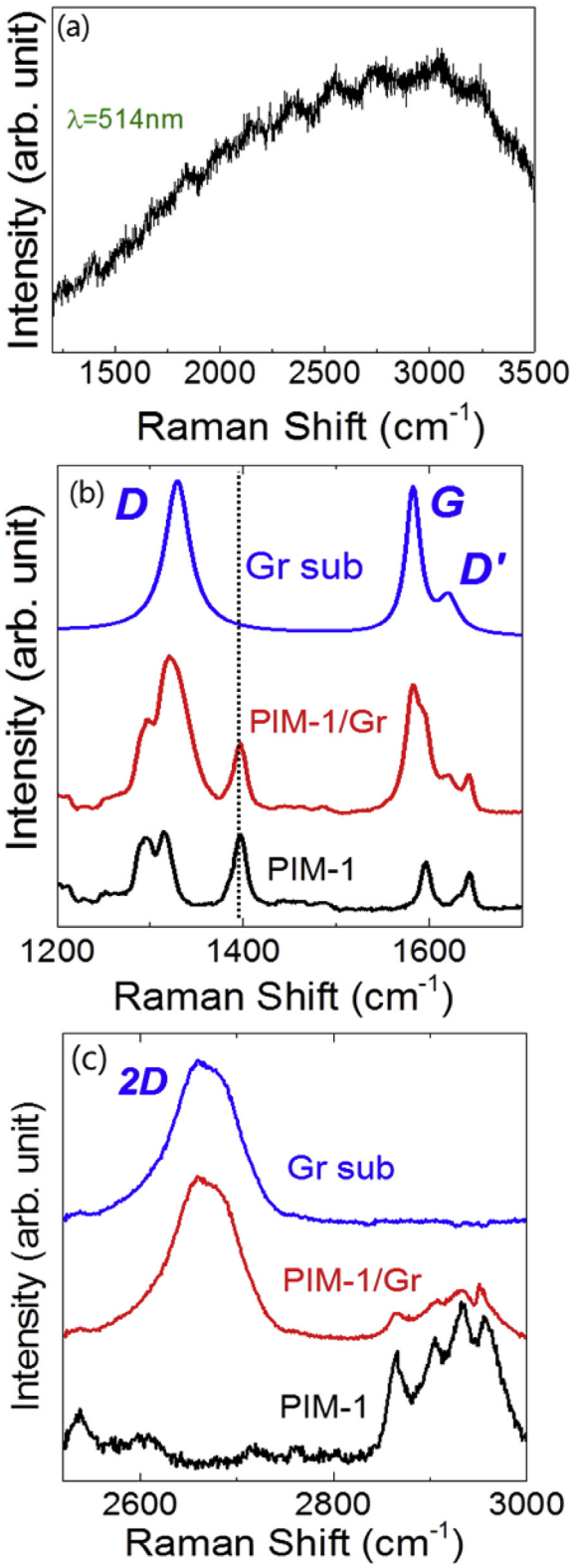

Fig. 7. Raman spectra of PIM-1/Gr composite samples measured at (a) 514 nm and (b,c) 633 nm. Panels b and c also show the Raman spectrum of PIM-1 and the composite spectrum after PIM-1 signal was subtracted. (A colour version of this figure can be viewed online.)

3.3. STEM and EELS imaging

STEM investigations were performed on PIM-1/Gr membranes prepared by spin-coating the dispersions onto a glass side and then transferring the film onto a holey carbon TEM grid. The thickness of the membranes was optimised by careful control of the PIM-1 concentration in the spin coating solution as reported previously in Ref. [53]. Fig. 8(a–d) shows bright field (BF) STEM images (left) and the simultaneously acquired medium angle annular dark field (MAADF) STEM images (right) for graphene flakes embedded in free-standing PIM-1/Gr membranes. Comparing these two imaging modes, one can immediately note that the MAADF contrast is greater, allowing the morphology of the graphene flakes to be more clearly observed. The MAADF image intensity depends on the structure and the density of the material. In these composite membranes the PIM-1 matrix is amorphous, while the graphene flakes are crystalline. By optimal selection of the collection angle used for imaging, it is therefore possible to obtain a significantly higher intensity on the MAADF detector as a result of diffraction in the crystalline graphene material. The atomic number of both materials is similar but the greater density of the graphitic material (2.2 g/cm^3) compared to PIM-1 (0.9 g/cm^3) [23] also acts to increase the scattering to medium and high angles and hence improve the contrast of the MAADF compared to the BF image.

The membrane shown in Fig. 8(a–b) has a thickness of just 35 nm (see experimental method). The varying intensity of the graphene flakes in Fig. 8(b) indicates that different thicknesses are present in the membrane. Electron diffraction, shown in Fig. 9(c) reveals that the flakes are misoriented suggesting these are restacked rather than that the original graphite has not been exfoliated. As mentioned previously, the MAADF-STEM image in Fig. 9(a) offers better contrast than the BF-TEM image in Fig. 9(b). Close inspection of the flake morphology, also indicates that the flakes are folded and re-aggregated, which is most likely to have occurred prior to solvent evaporation during deposition of the PIM-1/Gr membrane. Fig. 8(c–d) displays BF- and MAADF-STEM images of graphene flakes within a 500 nm thick free-standing PIM-1/Gr membrane. In this case, the membrane is much thicker, allowing the graphene flakes to lie perpendicular to the plane of the film. The graphene flakes can be then imaged parallel to the basal plane. The disorder observed for these flakes when viewed side-on is consistent with the re-aggregation mentioned previously. Moreover, in both films the presence of large pores can be observed in close proximity to the graphene flakes (indicated by the arrows in Fig. 8(a–d). The pores shown in Fig. 8(a–b) are likely to have been formed during the formation of the membranes (evaporation of the solvent), while the ones in Fig. 8(c–d) are beam sensitive and likely to have been formed as a result of electron beam irradiation of the sample. In the thicker films the pores can be seen to lie at the interface between the basal plane of the graphene and the PIM-1 suggesting that the van-der-Waals interaction between the PIM-1 and the graphene flakes is the weakest point in the material.

Fig. 10 shows STEM-EELS imaging of a graphene flake embedded in a 35 nm thick PIM-1/Gr membrane. Analysis of the shape of the EELS C–K edge at an energy loss of 283 eV allows the planar sp^3 content to be measured using the method reported in Refs. [30] and [54]. For very thin specimens like these, the graphene flakes lie in the plane of the membrane. It follows that the measurement of the planar sp^3 content (see experimental method), is then sensitive to the number of layers in the graphene flakes because of the anisotropic distribution of the sp^3 bonding. Indeed, by optimising the experimental conditions to employ a large EELS collection angle of 62 mrad, we are able to probe scattering perpendicular to the electron beam [55], *i.e.* mainly the 1s to σ^* transition of the graphene flakes in our geometry. Consequently, the steps observed in

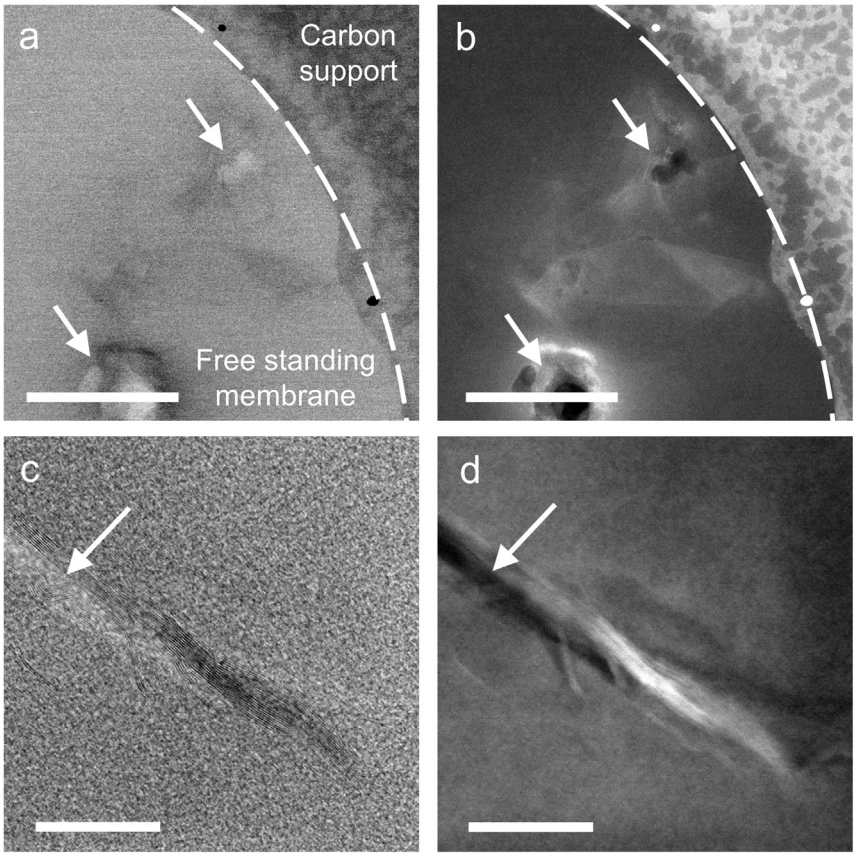

Fig. 8. (a,c) BF-STEM and (b,d) MAADF-STEM images of graphene flakes in a PIM-1 composite membrane showing folding of the graphene flakes and the formation of large pores in the regions of the PIM-1 film indicated by the arrows. In (a,b) the presence of the amorphous carbon TEM support grid can be seen top right. Scale bar in (1-b) and (c–d) are 200 nm and 20 nm, respectively.

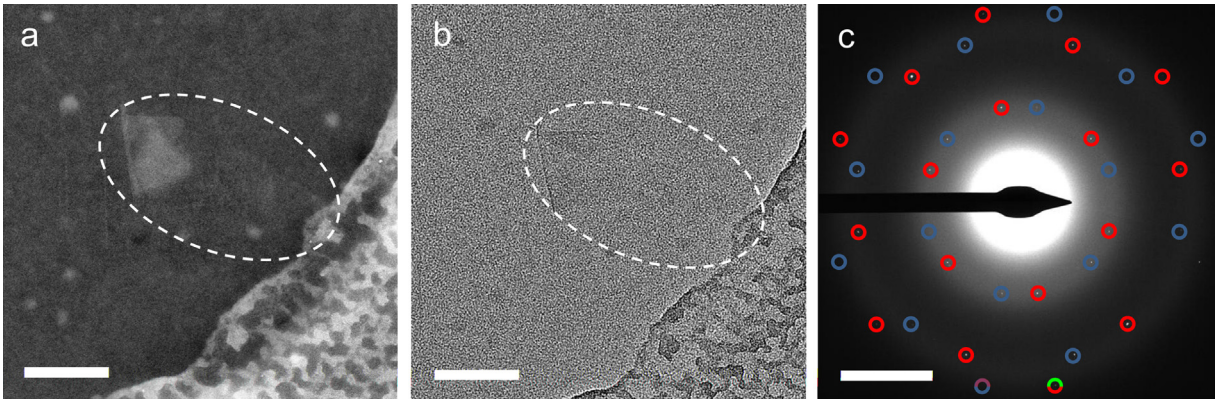

Fig. 9. (a) MAADF-STEM, (b) BF-TEM images and (c) the corresponding diffraction pattern of a graphene flakes in a PIM-1 composite membrane showing the flakes are misoriented, suggesting the re-stacking of the flakes. The dash line ellipse in (a–b) indicates the position of the flake. Scale in (a–b) and (c) are 100 nm and 5 nm^{-1}, respectively. (A colour version of this figure can be viewed online.)

the sp^3 planar content map (Fig. 10(b)) are directly related to the thickness of the graphene. Moreover, this method allows imaging the graphene flakes embedded in the polymer matrix with a high signal-to-background ratio. Fitted spectra corresponding to different positions within the spectrum image shown in Fig. 10(b) are displayed in Fig. 10(d–f). The σ^* intensity (filled green curve) is greater in the region of the sample containing a thick graphene flake than in regions where the graphene is thinner (Fig. 10(f)). The σ^* intensity is lower still in the areas of the sample containing only PIM-1 (Fig. 10(d)).

Figure 10(c) shows a high resolution BF-STEM image of the folded edge region in the area indicated by the small black dashed rectangle in Fig. 10(a). In this case, high resolution imaging allows confirmation of the graphitic nature of this flake and also the flake thickness to be determined as each fringe corresponds to an individual layer: this fold is observed to contain 12 graphene layers.

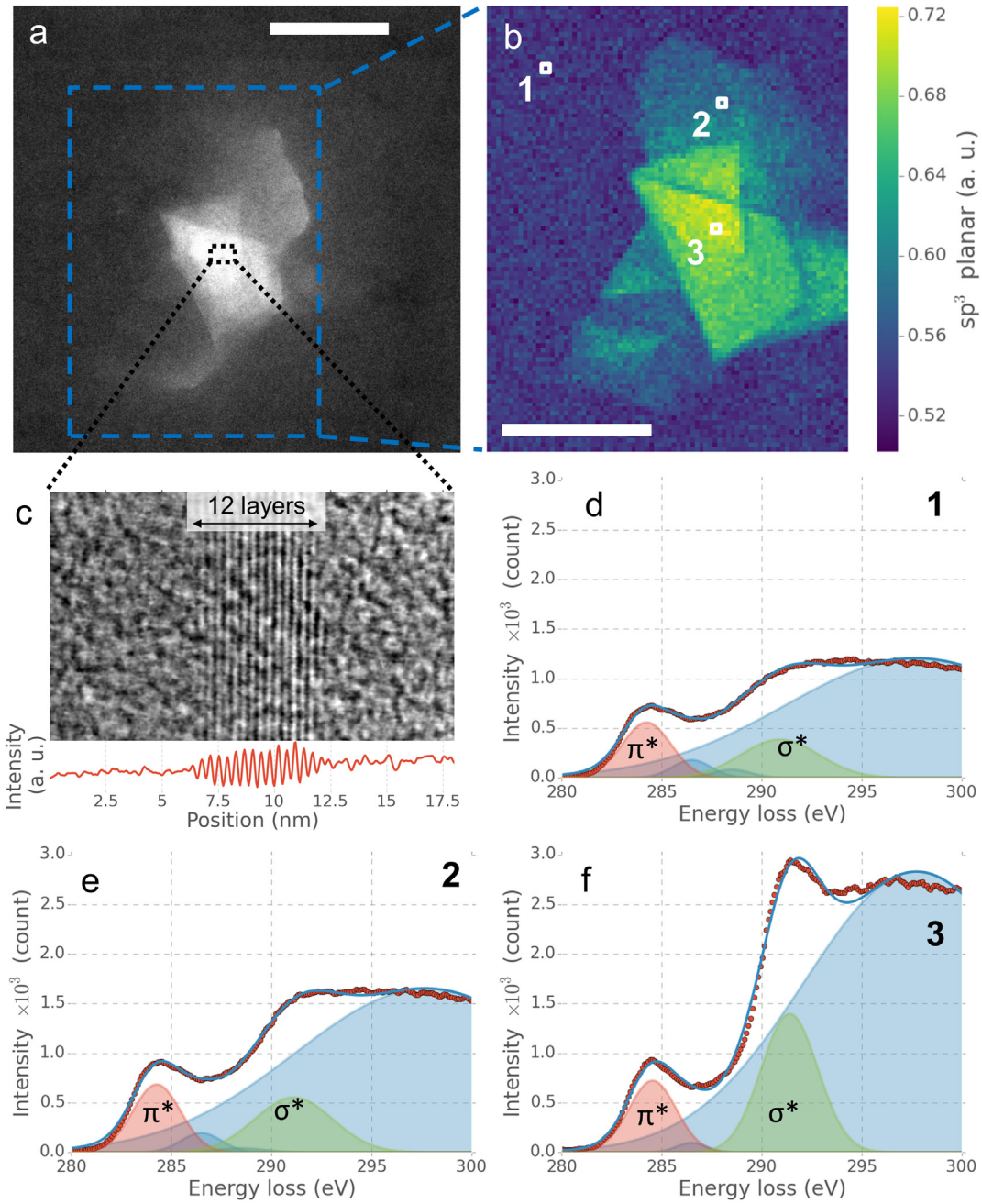

Fig. 10. STEM-EELS analysis of folded and restacked graphene flakes within a PIM-1/Gr composite membrane: (a) MAADF-STEM image (b) Map showing the intensity of the sp^3 bonding component of the C–K edge for the area marked by the large blue dashed rectangle in (a). (c) High resolution BF-STEM image of the area marked with the small black dashed rectangle in (a) showing a folded edge region. The fold allows the thickness in this area to be determined as 12 layers. (d–f) Fit of the C–K edge for different positions within the spectrum image. The experimental data and the model are plotted with red dots and a blue line, respectively. The filled curves correspond to the five Gaussian functions used in the fitting model. The scale bar in (a–b) corresponds to 100 nm. (A colour version of this figure can be viewed online.)

4. Conclusions

We have demonstrated the first detailed characterisation of PIM-1/graphene composite membranes by using complementary techniques such as UV–Vis spectroscopy, Raman spectroscopy, STEM imaging and EEL spectroscopy. UV–Vis spectroscopy allowed the graphene concentration to be determined, revealing that greater exfoliation yield was obtained for low initial graphite concentrations. We have demonstrated that the presence of PIM-1 enhances the direct exfoliation of graphene in chloroform, although the efficiency of the process and stability of the resulting dispersion strongly depends on the graphene concentration. Chloroform is known to be a poor solvent for liquid-phase exfoliation [8], therefore we also investigated the use of N-Methyl-2-pyrrolidone (NMP). NMP-based graphene dispersions were added to the monomers and polymerization in NMP was performed. However, the process failed as the right molar mass could not be reached and graphene was also observed to oxidize, due to the relatively high temperature needed for polymerization. The limited choice of solvents may raise issues on the scalability of the process.

Raman spectroscopy for these materials is challenging because of PIM-1's strong photoluminescence. However, by selecting a laser

wavelength of 633 nm, it is possible to clearly observe the 2D peak of graphene, which provides information on the thickness of the material. STEM allows the distribution and morphology of the nanosheets to be investigated at higher spatial resolution than is possible using Raman spectroscopy. We have demonstrated that high signal-to-background images of the flakes can be obtained using MAADF and EELS, where the EEL spectrum images are formed using the sp^3 planar content of the C–K edge. Together with complementary electron diffraction data, these images provide further information on the local morphology and thickness of the nanosheets. Both Raman Spectroscopy and STEM characterisation revealed that the composite PIM-1 membranes produced in this work contained no monolayer graphene material, but did contain folded and re-stacked few layer graphene nanosheets (3–15 layers thick) with lateral size of ~100–300 nm. Our results indicate that there is strong re-stacking of initially exfoliated graphene in solution when forming the composite. This is expected to produce strong changes in the mechanical properties and the physical aging of the membrane.

Acknowledgements

This work was supported by the Engineering and Physical Sciences Research Council, in the framework of the project Graphene-Based Membranes (EP/K016946/1). SJH and EP also acknowledge support from the US Defense Threat reduction agency (grant HDTRA1-12-1-0013) - and EPSRC imaging platform grant (EP/M010619/1). KA is supported by the Deanship of Graduate Studies and Research, Taibah University, Saudi Arabia. EP acknowledges Fredrik Hage from SuperSTEM Laboratory for discussion on the EELS analysis and for providing the starting python script. KGZ acknowledges The Royal Society in the framework of the Newton Fellowship scheme.

References

[1] A.K. Geim, K.S. Novoselov, The rise of graphene, Nat. Mater 6 (3) (2007) 183–191.
[2] A.H. Castro Neto, N.M.R. Peres, K.S. Novoselov, A.K. Geim, The electronic properties of graphene, Rev. Mod. Phys. 81 (1) (2009) 109–162.
[3] X. Du, I. Skachko, A. Barker, E.Y. Andrei, Approaching ballistic transport in suspended graphene, Nat. Nano 3 (8) (2008) 491–495.
[4] K.S. Novoselov, A.K. Geim, S.V. Morozov, D. Jiang, Y. Zhang, S.V. Dubonos, et al., Electric field effect in atomically thin carbon films, Science 306 (5696) (2004) 666–669.
[5] A.A. Balandin, S. Ghosh, W. Bao, I. Calizo, D. Teweldebrhan, F. Miao, et al., Superior Thermal Conductivity of Single-Layer Graphene, Nano Lett. 8 (3) (2008) 902–907.
[6] C. Lee, X. Wei, J.W. Kysar, J. Hone, Measurement of the elastic properties and intrinsic strength of monolayer graphene, Science 321 (5887) (2008) 385–388.
[7] K.S. Novoselov, V.I. Fal'ko, L. Colombo, P.R. Gellert, M.G. Schwab, K. Kim, A roadmap for graphene, Nature 490 (7419) (2012) 192–200.
[8] Y. Hernandez, V. Nicolosi, M. Lotya, F.M. Blighe, Z. Sun, S. De, et al., High-yield production of graphene by liquid-phase exfoliation of graphite, Nat. Nanotechnol. 3 (9) (2008) 563–568.
[9] K.R. Paton, E. Varrla, C. Backes, R.J. Smith, U. Khan, A. O'Neill, et al., Scalable production of large quantities of defect-free few-layer graphene by shear exfoliation in liquids, Nat. Mater 13 (6) (2014) 624–630.
[10] J.N. Coleman, M. Lotya, A. O'Neill, S.D. Bergin, P.J. King, U. Khan, et al., Two-dimensional nanosheets produced by liquid exfoliation of layered materials, Science 331 (6017) (2011) 568–571.
[11] H. Yang, F. Withers, E. Gebremedhn, E. Lewis, L. Britnell, A. Felten, et al., Dielectric nanosheets made by liquid-phase exfoliation in water and their use in graphene-based electronics, 2D Mater. 1 (1) (2014) 011012.
[12] N.B. McKeown, P.M. Budd, Polymers of intrinsic microporosity (PIMs): organic materials for membrane separations, heterogeneous catalysis and hydrogen storage, Chem. Soc. Rev. 35 (8) (2006) 675–683.
[13] P.M. Budd, N.B. McKeown, D. Fritsch, Free volume and intrinsic microporosity in polymers, J. Mater. Chem. 15 (20) (2005) 1977–1986.
[14] L.M. Robeson, The upper bound revisited, J. Membr. Sci. 320 (1–2) (2008) 390–400.
[15] P. Bernardo, E. Drioli, G. Golemme, Membrane gas separation: a review/state of the art, Industrial Eng. Chem. Res. 48 (10) (2009) 4638–4663.
[16] W. Fang, L. Zhang, J. Jiang, Polymers of intrinsic microporosity for gas permeation: a molecular simulation study, Mol. Simul. 36 (12) (2010) 992–1003.
[17] P.M. Budd, E.S. Elabas, B.S. Ghanem, S. Makhseed, N.B. McKeown, K.J. Msayib, et al., Solution-processed, organophilic membrane derived from a polymer of intrinsic microporosity, Adv. Mater. 16 (5) (2004) 456–459.
[18] M. Žák, M. Klepic, L.Č. Šťastná, Z. Sedláková, H. Vychodilová, Š. Hovorka, et al., Selective removal of butanol from aqueous solution by pervaporation with a PIM-1 membrane and membrane aging, Sep. Purif. Technol. 151 (2015) 108–114.
[19] D. Fritsch, P. Merten, K. Heinrich, M. Lazar, M. Priske, High performance organic solvent nanofiltration membranes: Development and thorough testing of thin film composite membranes made of polymers of intrinsic microporosity (PIMs), J. Membr. Sci. 401 (2012) 222–231.
[20] T. Anokhina, A. Yushkin, P. Budd, A. Volkov, Application of PIM-1 for solvent swing adsorption and solvent recovery by nanofiltration, Sep. Purif. Technol. 156 (2015) 683–690.
[21] S. Harms, K. Rätzke, F. Faupel, N. Chaukura, P. Budd, W. Egger, et al., Aging and free volume in a polymer of intrinsic microporosity (PIM-1), J. Adhesion 88 (7) (2012) 608–619.
[22] T. Koschine, K. Rätzke, F. Faupel, M.M. Khan, T. Emmler, V. Filiz, et al., Correlation of gas permeation and free volume in new and used high free volume thin film composite membranes, J. Polym. Sci. Part B Polym. Phys. 53 (3) (2015) 213–217.
[23] A. Gonciaruk, K. Althumayri, W.J. Harrison, P.M. Budd, F.R. Siperstein, PIM-1/graphene composite: a combined experimental and molecular simulation study, Microporous Mesoporous Mater. 209 (2015) 126–134.
[24] M.M. Khan, V. Filiz, G. Bengtson, S. Shishatskiy, M.M. Rahman, J. Lillepaerg, et al., Enhanced gas permeability by fabricating mixed matrix membranes of functionalized multiwalled carbon nanotubes and polymers of intrinsic microporosity (PIM), J. Membr. Sci. 436 (2013) 109–120.
[25] N.B. McKeown, Polymers of intrinsic microporosity, ISRN Mater. Sci. 2012 (2012) 513986.
[26] F. Bonaccorso, A. Lombardo, T. Hasan, Z. Sun, L. Colombo, A.C. Ferrari, Production and processing of graphene and 2d crystals, Mater. Today 15 (12) (2012) 564–589.
[27] U. Khan, A. O'Neill, M. Lotya, S. De, J.N. Coleman, High-concentration solvent exfoliation of graphene, Small 6 (7) (2010) 864–871.
[28] M. Lotya, Y. Hernandez, P.J. King, R.J. Smith, V. Nicolosi, L.S. Karlsson, et al., Liquid phase production of graphene by exfoliation of graphite in surfactant/water solutions, J. Am. Chem. Soc. 131 (10) (2009) 3611–3620.
[29] M. Lotya, P.J. King, U. Khan, S. De, J.N. Coleman, High-Concentration, Surfactant-Stabilized Graphene Dispersions, Acs Nano 4 (6) (2010) 3155–3162.
[30] B. Mironov, H. Freeman, A. Brown, F. Hage, A. Scott, A. Westwood, et al., Electron irradiation of nuclear graphite studied by transmission electron microscopy and electron energy loss spectroscopy, Carbon 83 (2015) 106–117.
[31] Francisco de la Peña, Pierre Burdet, Tomas Ostasevicius, Mike Sarahan, Magnus Nord, Vidar Tonaas Fauske, et al., Hyperspy: HyperSpy 0.8.2, 2015, http://dx.doi.org/10.5281/zenodo.28025.
[32] T. Malis, S. Cheng, R. Egerton, EELS log-ratio technique for specimen-thickness measurement in the TEM, J. electron Microsc. Tech. 8 (2) (1988) 193–200.
[33] K. Iakoubovskii, K. Mitsuishi, Y. Nakayama, K. Furuya, Thickness measurements with electron energy loss spectroscopy, Microsc. Res. Tech. 71 (8) (2008) 626–631.
[34] J.N. Coleman, Liquid exfoliation of defect-free graphene, Acc. Chem. Res. 46 (1) (2013) 14–22.
[35] H.L. Cupples, The surface tension of chloroform: its variation with the composition of the gas phase, J. Phys. Chem. 50 (5) (1946) 412–417.
[36] P.M. Budd, K.J. Msayib, C.E. Tattershall, B.S. Ghanem, K.J. Reynolds, N.B. McKeown, et al., Gas separation membranes from polymers of intrinsic microporosity, J. Membr. Sci. 251 (1–2) (2005) 263–269.
[37] A. Schlierf, H. Yang, E. Gebremedhn, E. Treossi, L. Ortolani, L. Chen, et al., Nanoscale insight into the exfoliation mechanism of graphene with organic dyes: effect of charge, dipole and molecular structure, Nanoscale 5 (10) (2013) 4205–4216.
[38] Jorio A, Dresselhaus MS, Saito R, Dresselhaus G. Raman Spectroscopy in Graphene Related Systems: Wiley-VCH.
[39] A.C. Ferrari, D.M. Basko, Raman spectroscopy as a versatile tool for studying the properties of graphene, Nat. Nanotechnol. 8 (4) (2013) 235–246.
[40] A.C. Ferrari, J.C. Meyer, V. Scardaci, C. Casiraghi, M. Lazzeri, F. Mauri, et al., Raman spectrum of graphene and graphene layers, Phys. Rev. Lett. 97 (18) (2006) 4.
[41] A. Eckmann, A. Felten, A. Mishchenko, L. Britnell, R. Krupke, K.S. Novoselov, et al., Probing the nature of defects in graphene by Raman spectroscopy, Nano Lett. 12 (8) (2012) 3925–3930.
[42] A. Eckmann, A. Felten, I. Verzhbitskiy, R. Davey, C. Casiraghi, Raman study on defective graphene: effect of the excitation energy, type, and amount of defects, Phys. Rev. B (3) (2013) 88.
[43] S. Pisana, M. Lazzeri, C. Casiraghi, K.S. Novoselov, A.K. Geim, A.C. Ferrari, et al., Breakdown of the adiabatic Born–Oppenheimer approximation in graphene, Nat. Mater 6 (3) (2007) 198–201.
[44] T. Mohiuddin, A. Lombardo, R. Nair, A. Bonetti, G. Savini, R. Jalil, et al., Uniaxial strain in graphene by Raman spectroscopy: G peak splitting, Grüneisen

parameters, and sample orientation, Phys. Rev. B 79 (20) (2009) 205433.
[45] J. Zabel, R.R. Nair, A. Ott, T. Georgiou, A.K. Geim, K.S. Novoselov, et al., Raman spectroscopy of graphene and bilayer under biaxial strain: bubbles and balloons, Nano Lett. 12 (2) (2012) 617–621.
[46] C. Casiraghi, A. Hartschuh, H. Qian, S. Piscanec, C. Georgi, A. Fasoli, et al., Raman spectroscopy of graphene edges, Nano Lett. 9 (4) (2009) 1433–1441.
[47] H. Yang, Y. Hernandez, A. Schlierf, A. Felten, A. Eckmann, S. Johal, et al., A simple method for graphene production based on exfoliation of graphite in water using 1-pyrenesulfonic acid sodium salt, Carbon 53 (2013) 357–365.
[48] S. Haar, A. Ciesielski, J. Clough, H. Yang, R. Mazzaro, F. Richard, et al., A supramolecular strategy to leverage the liquid-phase exfoliation of graphene in the presence of surfactants: unraveling the role of the length of fatty acids, Small 11 (14) (2015) 1691–1702.
[49] A. Ciesielski, S. Haar, M. El Gemayel, H. Yang, J. Clough, G. Melinte, et al., Harnessing the liquid-phase exfoliation of graphene using aliphatic compounds: a supramolecular approach, Angew. Chem. Int. Ed. Engl. 53 (39) (2014) 10355–10361.
[50] S. Haar, M. El Gemayel, Y. Shin, G. Melinte, M.A. Squillaci, O. Ersen, C. Casiraghi, A. Ciesielski, P. Samorí, Enhancing the liquid-phase exfoliation of graphene in organic solvents upon addition of n-octylbenzen, Sci. Rep. 5 (2015) 16684.
[51] V. Carozo, C.M. Almeida, E.H. Ferreira, L.G. Cancado, C.A. Achete, A. Jorio, Raman signature of graphene superlattices, Nano Lett. 11 (11) (2011) 4527–4534.
[52] V. Carozo, C.M. Almeida, B. Fragneaud, P.M. Bedê, M.V.O. Moutinho, J. Ribeiro-Soares, et al., Resonance effects on the Raman spectra of graphene superlattices, Phys. Rev. B 88 (8) (2013) 085401.
[53] P. Gorgojo, S. Karan, H.C. Wong, M.F. Jimenez-Solomon, J.T. Cabral, A.G. Livingston, Ultrathin polymer films with intrinsic microporosity: anomalous solvent permeation and high flux membranes, Adv. Funct. Mater. 24 (30) (2014) 4729–4737.
[54] Zhang Z-l, R. Brydson, Z. Aslam, S. Reddy, A. Brown, A. Westwood, et al., Investigating the structure of non-graphitising carbons using electron energy loss spectroscopy in the transmission electron microscope, Carbon 49 (15) (2011) 5049–5063.
[55] G. Botton, A new approach to study bonding anisotropy with EELS, J. Electron Spectrosc. Relat. Phenom. 143 (2) (2005) 129–137.